

# Optimization of airgap in a monocentric lens assembly and metasurface based anti-reflecting coating in the long-wave IR regime

Manish Kala<sup>1</sup>, Pawan Singh<sup>1</sup>, Sanjay Kumar Mishra<sup>2</sup>, Unnikrishnan Gopinathan<sup>2</sup>, Ajay Kumar<sup>2</sup>, Akhilesh Kumar Mishra<sup>1, 3, \*</sup>

<sup>1</sup>*Department of Physics, Indian Institute of Technology Roorkee, Roorkee-247667, Uttarakhand, India*

<sup>2</sup>*Photonics Research Lab, Instruments Research and Development Establishment, Dehradun 248008, India*

<sup>3</sup>*Centre for Photonics and Quantum Communication Technology, Indian Institute of Technology Roorkee, Roorkee-247667, Uttarakhand, India*

*\*Corresponding author: [akhilesh.mishra@ph.iitr.ac.in](mailto:akhilesh.mishra@ph.iitr.ac.in)*

## Abstract

Owing to minimal aberration, larger field-of-view, and high resolution, monocentric lenses are preferred over other imagers in hemispherical image surface scenarios, particularly in the long-wave infrared (LWIR) region. Herein, we study a monocentric lens assembly consisting of a ball lens and two hemispherical shell lenses of given radii of curvature and lens materials to enhance the transmission of LWIR ranging from  $8\mu\text{m}$  to  $12\mu\text{m}$  wavelength. We optimize the air gaps between the lenses of the assembly for a wider range of incidence angles assuming antireflecting coating (ARC) on all surfaces of the lenses. Additionally, the effect of temperature variation on the transmittance is also studied to attain an optimum air gap between the lenses. With the variation in incidence angle and temperature, modulations in focal length and spot size are reported for different wavelengths. Further, we propose a metasurface design to replace conventional multilayer ARCs to enhance the transmittance through the lens assembly over the given wavelength range for a wide field-of-view.

**Keywords:** Monocentric lens, anti-reflecting coating, LWIR, temperature, metasurface.

## 1. Introduction

The imaging technology has witnessed a rapid continuous growth over the last few decades. In particular, applications such as in aircraft monitoring, surveillance, communications, agriculture, forensics, etc. demand a wide field-of-view (FOV) imagers along with higher-resolution images [1-6]. To achieve higher resolutions, it is required to match the resolution of the optics to that of the detector. This in turn maximizes the information throughout of the imaging system quantified by Space Bandwidth Product (SBP). Due to rapid advances in detector technology, the designer often faces the challenge of designing optics with resolving powers that match detector resolution. One of the strategies to increase the resolution and thereby SBP for a given FOV is to scale the optical system (optics and the detector). If one assumes that the optical system is diffraction limited, the scaling by a factor of  $M$ , leads to an increase in Space Bandwidth Product (SBP) by a factor of  $M^2$ . Lohmann [7] pointed out that this scaling in SBP does not happen as the aberrations also scale up. Hence, aberrations limit an optical system from achieving performance (in terms of SBP often quantified by Shannon number) that it is capable of, and the performance degrades further as the FOV increases.

For high-resolution images, lens assembly must have a large numerical aperture to gather radiation efficiently and a large focal length to magnify the image with the least aberrations [8]. Imagers having a ratio of aperture to the square of operating wavelength of more than 1000 show higher aberrations and poor image quality. Hence, aberration control has been central to the strategies to achieve higher resolutions over wider FOV as desired in Gigapixel imaging systems. One of the traditional approaches has been to balance out aberrations by adding more optical surfaces. This approach has been used successfully in applications like lithography systems, but the downside is that it increases the size and weight of optics which is critical for systems to be used for outdoor applications as in the case of surveillance systems. To overcome the problem, a wide-field objective lens is associated with cameras with multiple narrow-field micro cameras which reduces aberration in the images. The large aperture of micro camera can resolve the problem of aberration but requires a complex optical system. Moreover, the small aperture size of the micro camera faces a problem while capturing the incoming radiation [9-11]. When the optics is scaled up, the resolution increases as well as FOV increases but in this case, it becomes difficult to control the aberration in wide FOV.

Instead of using a complex optical system, a spherical lens provides flexibility for wide-angle high-resolution imaging. Usually, the design of fish-eye-like lenses is complicated due to short focal lengths and lower radiation capturing ability as well as aberrations, and hence, it fails to provide wide-angle high-resolution images. For wider FOV, monocentric lens assembly, which is a combination of a spherical lens (ball lens) and multiple spherical or hemispherical shells is used. Due to the common center of refracting surfaces, nodal points, principal points, and optical center lie at the same point and such assembly does not face coma and astigmatism [12]. Uniform curvature of the monocentric lens minimizes optical distortions and aberrations for wide FOV.

For achieving wider FOV with spherical surfaces, an early design of the monocentric lens was introduced by T. Sutton in 1859, but it had uncorrected aberrations and high  $f$ -number. To resolve these problems, in 1942, J. G. Baker suggested to use two different glasses with high (flint glass for shells) and low refractive indices (crown glass for core lens), which offered the correction in aberration and  $f$ -number [13].

In the multiscale imaging system, the use of monocentric lens assembly as objective lens was discussed by Ford and Tremblay [14]. In such a system, overlying parts of the spherical image surface are imparted onto image detectors or sensors which form the whole image by the combination of all images detected by multiple sub-imagers [14,15]. To achieve high-resolution panoramic images, a monocentric lens is very useful in which the image surface is detected by multiple sensors placed spherically. For optimum transmittance through the lens assembly, the aperture should be placed near sub-imagers and it has been also reported that lens assembly based on Galilean configuration deals better with aberrations in comparison to Keplerian configuration [16]. The FOV of sub-imagers must overlap efficiently for image formation [17,18].

In a monocentric lens, light can be controlled by a stop aperture at the center of the lens or by transfer optics and the image is supposed to be formed on the curved surface but due to the complex design of a curved detector or the unavailability of the detector, a large number of flat surfaces are used to form the curved image surface. Alternatively, it can be done by imaging the fiber bundle with curved input and flat output surface [19]. Stamenov et al. demonstrated angle-independent resolution for conventional imagers for broad FOV, and they compared imaging and waveguide-

based transmission images through monocentric lenses [20]. They also described an easy design of a two-glass symmetric lens that can be focused on only axial translation.

Mostly, two-glass system (2GS) monocentric lens works well for wide FOV. The 2GS-based monocentric lens assembly displays a cutting-edge innovation in optical and thermal imaging that enhances visual performance by the integration of two IR glasses within a single assembly for versatile applications [19-21]. However, to obtain ultrawide FOV, multiscale imaging system based on concentric lenses are used. Using a catadioptric multi-scale system with spherical mirror having focal length of 72mm,  $F=2$ , FOV as wide as  $360^\circ \times 1^\circ$  can be achieved for LWIR region (8-12 $\mu\text{m}$ ) with minimum distortion ( $<5\%$ ) [22]. To minimize the aberration, Uniyal et al. proposed a multiscale monocentric lens imager using first order optics for LWIR region which covers  $80^\circ \times 16^\circ$  FOV over five detector arrays [23].

Monocentric lens being a critical component in the design of wide FOV high resolution imaging systems, the design, fabrication and assembly of monocentric lens assemblies are of critical importance. An addition issue in IR domain is unavailability of the glue to paste lenses. This makes the realization of such monocentric lens assembly in LWIR region difficult as leaving air gap between two lenses becomes indispensable. This paper seeks to address this research gap. Since refractive indices of air and lens material are very different, the associated transmittance losses are huge. Hence the air gap optimization is essential to optimize transmission in such systems.

Uniform and high transmittance of the incident radiation over wide angles is the qualifying criteria for the improvement of the visibility of images through any lens system. Herein, we numerically optimize the air gaps between the lenses in a two-glass monocentric lens assembly of given radii of curvature and lens materials. The lenses of the assembly are assumed to be coated with ARCs to achieve maximum transmittance. The lens assembly operating in the long-wave infrared (LWIR) region (8  $\mu\text{m}$  to 12  $\mu\text{m}$  wavelength) encounters the problem of low transmittance and distortion through lenses due to large refractive index contrast. To enhance the transmittance, the air gaps between ARCs are primarily optimized to prevent the collapse of material stability with temperature variations. In this work, we consider a monocentric lens with IG6 glass as a core lens and two hemispherical shells made up of Ge for LWIR radiation for wide FOV. The effect of temperature variation is also discussed which further optimizes the air gap and output transmittance thereby. Additionally, we propose a robust thermally stable metasurface design on the lens surfaces holding potential of replacing conventional ARCs.

## **2. Monocentric lens configuration**

Monocentric lens assembly consists of one spherical core lens (also called ball lens) and two concentric hemispherical shells as shown schematically in Fig. 1. We have considered the core lens ( $L_2$ ) of material IG6 and hemispherical shells ( $L_1$  &  $L_3$ ) of Ge. The spherical core lens  $L_2$  is sandwiched between two hemispherical surfaces or lenses  $L_1$  and  $L_3$  as shown schematically in Fig.1a. The lens assembly focuses the incident rays on a spherical plane placed after lens  $L_3$  at focal length of the lens assembly (see Fig. 1b).

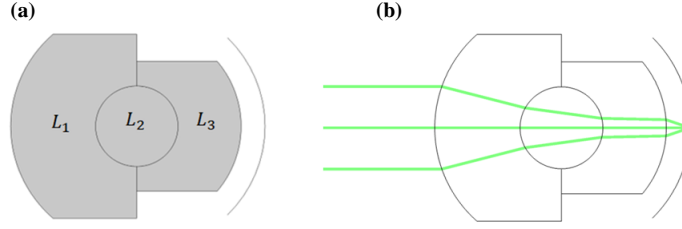


**Fig. 1:** (a) Schematic of the monocentric lens assembly, (b) focusing of rays on a spherical image plane. In lens assembly,  $L_2$  represents ball lens (IG6), and  $L_1$  &  $L_3$  are hemispherical lenses (Ge).

As shown in Fig. 2, we have also considered an air gap between core lens  $L_2$  and two internal surfaces of hemispherical shells ( $L_1$  &  $L_3$ ). Both internal and external surfaces of all the lenses are assumed to be coated with anti-reflecting coatings (ARCs).

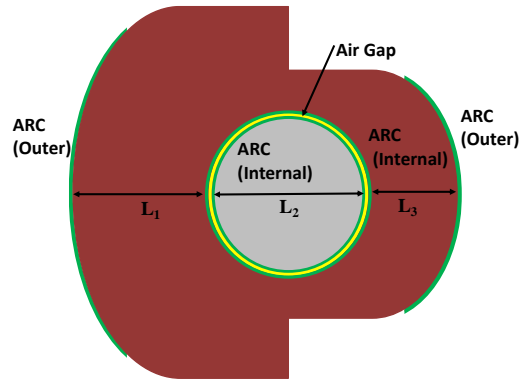


**Fig. 2:** Representation of monocentric lens assembly with an air gap (yellow) and with internal and outer ARCs (green), lenses  $L_1$  &  $L_3$  are in magenta and while  $L_2$  is represented by gray colour.

The combination of the three lenses covers a wide FOV for LWIR radiation ( $8\text{ }\mu\text{m} - 12\text{ }\mu\text{m}$ ). In our calculation, we have considered two hemispherical shells  $L_1$  and  $L_3$  with radii of curvature (ROC) 88.75 mm and 73.05 mm, respectively, while the core lens  $L_2$  has ROC of 28.35 mm. The lens assembly parameters are listed in Table 1.

**Table 1:** The parameters of the monocentric lens assembly

Lens	ROC (mm)	Diameter (mm)	Material
$L_1$	$R_1 = 88.75$ (left) $R_2 = 28.35$ (right)	150	Ge
$L_2$	$R_1 = 28.35$ (left) $R_2 = 28.35$ (right)	56.7	IG6
$L_3$	$R_1 = 28.35$ (left) $R_2 = 73.05$ (right)	108.3	Ge

The refractive indices of Ge and IG6 are taken from refs. [24, 25]. ARC thickness on the surfaces of lenses are assumed to be  $1.25\text{ }\mu\text{m}$ .

We calculate transmittance of monocentric lens assembly using COMSOL<sup>®</sup> Multiphysics software [26]. In the design of lens assembly, the diameter of aperture or entrance pupil is kept to be 52 mm

and for overlapping angular positions, the entrance pupil size is kept fixed at 91.7 mm. For studying transmittance with air gap variation, all the interfaces are assumed to have ARCs with transmittance of 97%. Initially, air gap is considered to be 10  $\mu\text{m}$  between internal ARCs of IG6 ball lens and Ge hemispherical lenses, and we consider the IR radiation with wavelength ranging from 8  $\mu\text{m}$  to 12  $\mu\text{m}$  for the wide incident angles. Moreover, we have calculated the transmittance with two distinct designs of metasurface on IG6 and Ge lenses replacing traditional multilayer ARCs.

### 3. Results and discussion

The optimization study of monocentric lens assembly is divided in the three subsections. In the first subsection, we study of the transmittance of IR radiation through lens assembly with varying air gap between internal ARCs. In the second subsection, we highlight the effect of temperature variation on the transmission of IR radiation, focal length, and spot size for various incident angles from input grid. Two different metasurface designs proposed to replace the conventional ARCs, are detailed in the third sub section.

To perform the simulation studies, we have used finite element method based COMSOL<sup>®</sup> Multiphysics platform and optimized 3D geometry (see Fig 3a). The discretized geometry of lenses is shown in Fig. 3b. For release of rays on lens assembly, we have considered a circular grid of diameter of 52 mm such that the center of grid and monocentric lens are on the same axis. The circular grid from source side and detector side are shown in Fig. 4 (a) and (b) respectively. The focusing of rays through the lens assembly is shown in Fig. 5, which show all the rays are focused on the center of image plane at focal length 91.7 mm.

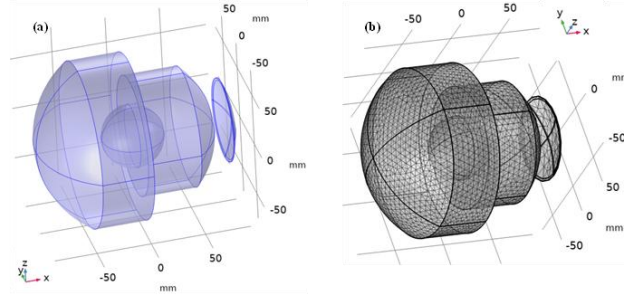


**Fig. 3:** (a) 3D geometry and (b) meshing of monocentric lens.

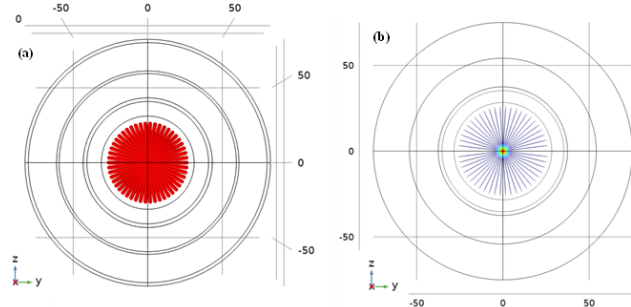


**Fig. 4:** Circular grid (a) source side to release the rays (b) detector side to receive the rays.

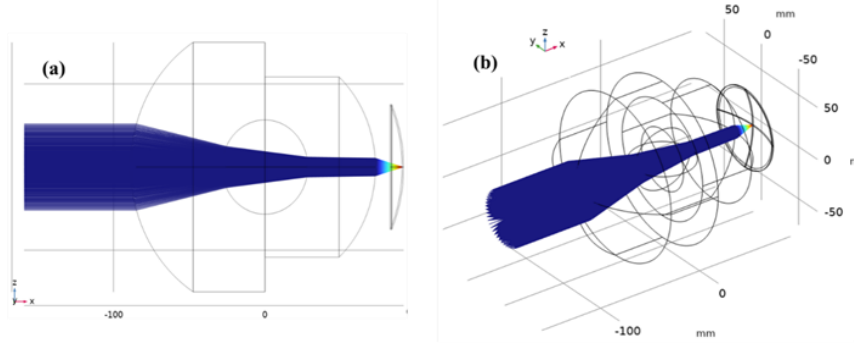


**Fig. 5:** Focusing of rays on the curved screen behind the lens at 91.7 mm distance from center (a) 2D view (b) 3D view.

### 3.1 Variation of transmittance of IR transmittance with air gap

For optimizing transmittance, we have calculated the transmittance with air gap variation as shown in Fig. 6 at normal incidence. At  $10\ \mu\text{m}$  wavelength, the transmittance maximizes to 58% for  $2.5\ \mu\text{m}$  air gap and further increase in air gap leads to oscillation in transmission. We noticed that the average (over wavelength) transmittance almost remains constant (maximum 53.7%) for the wavelength range  $8 - 12\ \mu\text{m}$ .

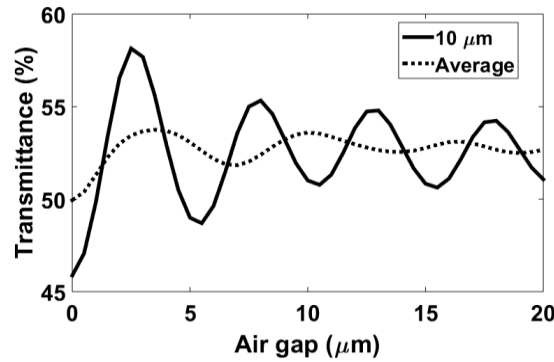


**Fig. 6:** Transmittance of  $10\ \mu\text{m}$  wavelength, and average transmittance over all wavelengths ( $8 - 12\ \mu\text{m}$ ) with air gap for normal incidence. Solid and dashed lines show the transmittance for  $10\ \mu\text{m}$  wavelength and average transmittance over wavelength range  $8 - 12\ \mu\text{m}$ , respectively.

Next, we study the effect of the variation of angle of incidence on transmittance. The average transmittance over all wavelengths ( $8 - 12\ \mu\text{m}$ ) at different angles of incidence ( $0^\circ$ ,  $2^\circ$ ,  $4^\circ$ ,  $6^\circ$ , and  $8^\circ$ ) are shown in Fig. 7 (a). From the figure, it is clear that the average transmittance decreases with increasing angles of incidence. At normal incidence, lens assembly shows about 53.7% average transmission. A comparative study of average transmittance over all angles of incidence for  $10\ \mu\text{m}$  and averaged over  $8 - 12\ \mu\text{m}$  wavelengths are shown in Fig. 7b. The figure explains that average transmittance at  $10\ \mu\text{m}$  wavelength averaged over all angles of incidence is 52.7 % at  $2.5\ \mu\text{m}$  air gap, while the wavelength average transmittance over all angles for IR radiation ( $8 - 12\ \mu\text{m}$ ) is only 48.3% at  $2\ \mu\text{m}$  air gap. The variation in spot size and transmittance for the lens assembly are given in supplementary [25].

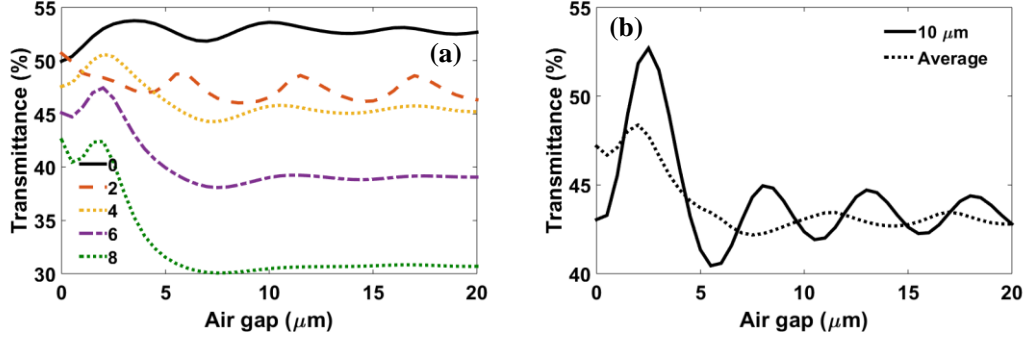


**Fig. 7:** (a) Variation of average transmittance over all wavelengths (8 – 12 μm) with air gap at different incidence angles and (b) solid and dashed lines show the angle averaged transmittance for 10 μm wavelength and wavelength averaged transmittance over wavelength range 8 – 12 μm, respectively.

As an extension of this study, we also examine the effect of temperature variation (ranging from 0°C to 40°C) on the transmittance of the lens assembly. As the temperature increases, the refractive indices and the radii of ball and hemispherical lenses vary, which in turn alters the air gap between the lenses. Hence, the temperature variation leads to variation in the transmittance. In addition, temperature variation also changes focal length and spot size, which are detailed in the supplementary [27].

### 3.2 Effect of temperature on transmittance of IR radiation

To study the temperature dependence of the transmittance, we have considered the wavelength as well as temperature-dependence of the refractive indices of IG6 and Ge, while ARCs are assumed to be independent of the temperature variation. Initially, we assumed 10 μm air gap, which of course varies with the temperature. With increase in the temperature, the refractive indices of Ge and IG6 increase linearly, while it decreases with increase in the wavelength [24, 25].

In the lens assembly, temperature not only affects the refractive indices, but it also alters the thicknesses of lenses. The expansion of lens thickness ( $d$ ) can be studied using  $d = d_0 + d_0\alpha(T_m - T_0)$ , which shows that the thickness of the lens increases linearly, where  $T_m$ ,  $T_0$ , and  $\alpha$  are operating temperature, reference temperature (20°C) and the coefficient of thermal expansion of the material, respectively [28]. The expansions of Ge and IG6 with temperature are shown in Figure 8 (a). On increasing the temperature, the outer surface of IG6 grows more rapidly than the internal surface of Ge lens. As both materials expand, the air gap between ARCs decreases gradually (see Fig. 8 (b)). Therefore, the optimization of the air gap is crucial to prevent damage of ARCs due to lens contact and the mechanical stability of the assembly.

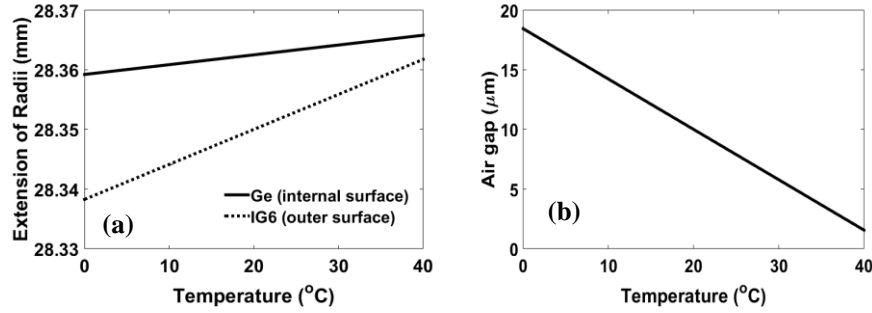


**Fig. 8:** (a) Thermal expansion of Ge (internal surface) and IG6 (outer surface), and (b) reduction of the air gap (initial gap 10  $\mu\text{m}$ ) with temperature.

To avoid the collapse of internal ARCs, we have considered the air gap to be 10  $\mu\text{m}$  initially. Fig 8 (b) shows that reduction of the air gap with temperature up to 40°C, where the air gap has reduced to 1.55  $\mu\text{m}$ . Also, if we reduce the temperature, then the air gap increases due to the contraction of the lens materials and at 0°C, we have 18  $\mu\text{m}$  air gap between the two lens surfaces as depicted in Fig 8 (b).

On comparing the average transmittance of lens assembly over wavelength range 8 – 12  $\mu\text{m}$  as shown in Fig. 9 (a), we note that as the incident angle increases, the average transmittance decreases down to 24% (for 8° incident angle) and it maximizes to 49.5% for normal incidence. If we take the average over all wavelengths and all incident angles, the transmittance is found 37%, but it exhibits a sudden increase if we increase the temperature beyond 30°C due to larger effective optical path length for a wider incidence angle. At 40°C temperature, the transmittance is calculated to be ~ 45% due to reduced air gap, as shown in Fig. 9 (b).

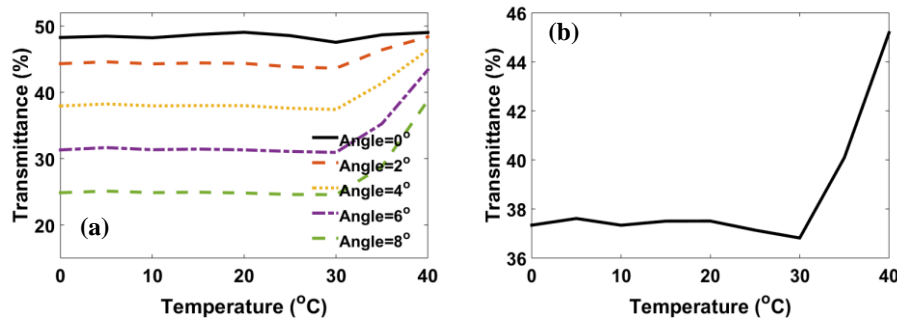


**Fig. 9:** (a) Averaged transmittance over all wavelengths for difference angle, and (b) average transmittance over all wavelengths and all angles incidence with increasing temperature.

Apart from affecting the transmittance, the temperature also alters the size of the focal spot and focal length, which are tabulated in Tables 2 and 3. From the tables, it can be observed that the focal length increases with temperature but it decreases with incident angles, whereas spot size increase with both temperature and incidence angle.

A representative focal spot and focal plane at 10  $\mu\text{m}$  wavelength and 20°C temperature for normal incidence is shown in Fig. 10. The relevant parameters are also given in the figures.

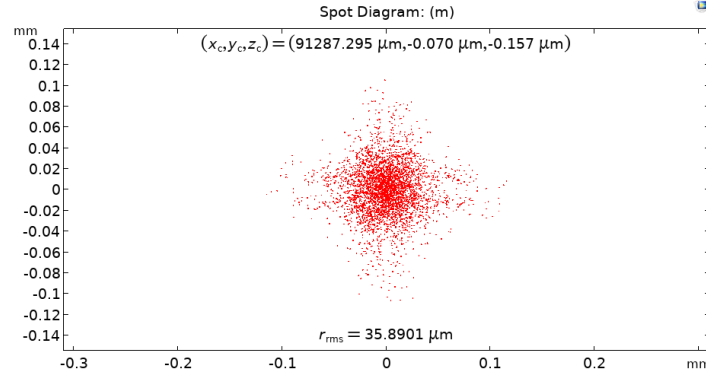


**Fig. 10:** Focal spot size at  $10\mu\text{m}$  wavelength at  $20^\circ\text{C}$  for normal incidence.

**Table 2:** RMS value of focus spot size on image surface at  $10\mu\text{m}$  wavelength for different incident angles

		Calculated RMS value of Focus spot ( $\mu\text{m}$ ) at $10\mu\text{m}$ wavelength		
S. No.	Temperature ( $^\circ\text{C}$ )	Angle of incidence= $0^\circ$	Angle of incidence= $4^\circ$	Angle of incidence= $8^\circ$
1	0	35.89	35.76	48.23
2	5	35.89	35.88	48.04
3	10	35.86	35.73	47.90
4	15	36.05	35.83	47.74
5	20	36.00	35.78	47.57
6	25	36.14	35.82	47.57
7	30	36.31	35.75	47.37
8	35	36.14	35.81	47.06
9	40	36.33	35.77	47.05

**Table 3:** Focal length of lens assembly at  $10\mu\text{m}$  wavelength for different incident angles

		Calculated focal length (mm) at $10\mu\text{m}$ wavelength		
S. No.	Temperature ( $^\circ\text{C}$ )	Angle of incidence= $0^\circ$	Angle of incidence= $4^\circ$	Angle of incidence= $8^\circ$
1	0	91.28	91.08	90.57
2	5	91.31	91.15	90.60
3	10	91.34	91.17	90.63
4	15	91.37	91.21	90.66
5	20	91.40	91.24	90.69
6	25	91.44	91.28	90.73
7	30	91.49	91.31	90.76
8	35	91.51	91.33	90.79
9	40	91.55	91.36	90.82

### 3.3 Transmittance of lens assembly with different metasurfaces

Usually, in the LWIR region, very few transparent materials are available for imaging systems. Additionally, multilayer ARCs may suffer from thermal instability in a longer duration of use.

This motivated us to explore the possibilities of designing and fabricating ARCs out of the host/substrate material itself. In the following, we propose a design of a metasurface acts as an ARC as shown in Fig. 11.

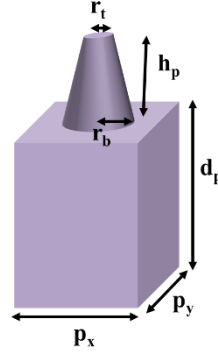


**Fig. 11:** An ARC design based on cone shape meta-structures.

In this design, we have considered  $p_x = p_y = 2 \mu\text{m}$ ,  $d_p = 6 \mu\text{m}$ , and the rest of the parameters are optimized for maximum transmittance at normal incidence. For our calculation, we have chosen  $r_b = 0.99 \mu\text{m}$ ,  $r_t = 100 \text{ nm}$ , and  $h_p = 3.44 \mu\text{m}$  for the air to Ge interface. For the interface of air to Ge, the transmittances are shown in Fig. 12. From the figure, it can be seen that the transmittance remains more than 95% up to  $30^\circ$  angle for both TE and TM modes. The increase in the transmittance is attributed to the Kerker effect, which arises from the interference of electric and magnetic dipole resonances [29].

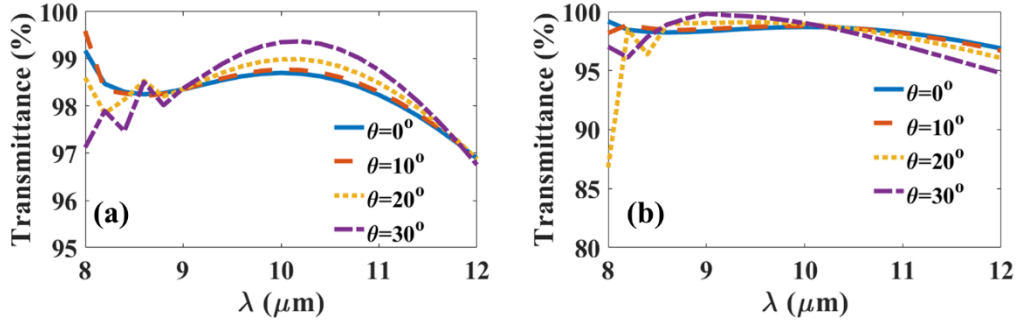


**Fig. 12:** Transmittance plots, for air to Ge interface for wider incidences (a) TE mode, and (b) TM mode.

Similarly, for air to IG6 interface, the optimized parameters are  $r_p = 0.99 \mu\text{m}$ ,  $w_p = 100 \text{ nm}$ , and  $h_r = 3.94 \mu\text{m}$ . The interface of air to IG6 also shows similar trends as reported in Fig. 13. The transmittances for both modes are more than 96% for wide field of view.

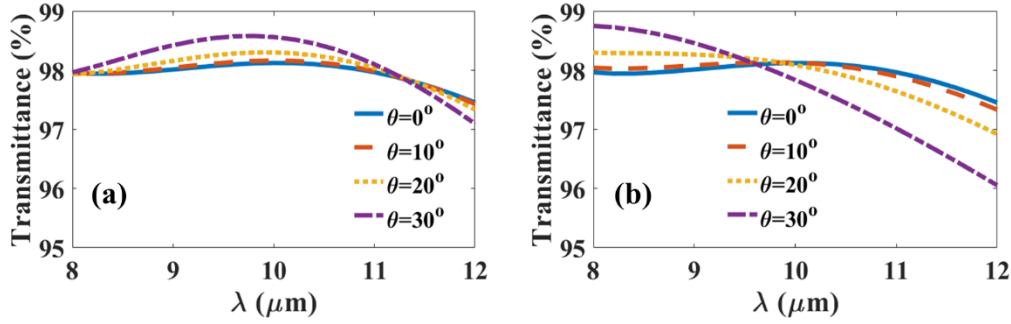


**Fig. 13:** Transmittance plots for air to IG6 interface for wider incidences (a) TE mode, and (b) TM mode.

Additionally, we also study the effect of these microstructures on Ge-IG6 interface with airgaps  $d = 1 \mu\text{m}$ ,  $2 \mu\text{m}$ ,  $3 \mu\text{m}$ ,  $4 \mu\text{m}$  and  $5 \mu\text{m}$  at normal incidence. The schematic of the structure is given in Fig. 14 (a). Fig. 14 (b) illustrates that the transmittance is almost always larger than 90% over the entire wavelength range for different values of airgaps.

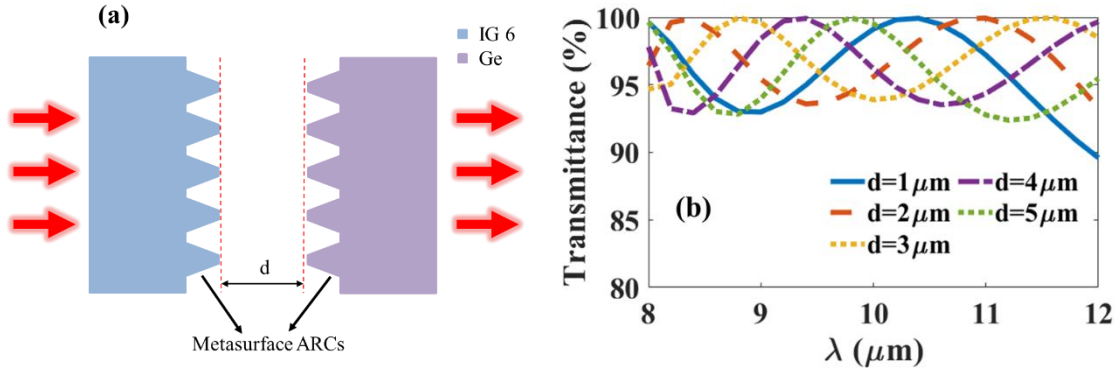


**Fig. 14:** (a) Schematic of the two lenses with metasurface ARCs and air gap, and (b) transmittance plots for IG6 to Ge interface for different widths of the airgap.

These studies establish that metasurface-based ARC has the potential to replace conventional ARCs. In addition, these microstructures can be grown on the lens surface with the lens material itself, which makes them more robust against environmental fluctuations.

## Conclusion

In this work, we studied the transmittance of IR radiation through monocentric lens assembly considering 97% transmitting ARCs on all surfaces. The air gap between ARCs was optimized to maximize the transmittance with variations in temperature, wavelength and incident angles. With  $10 \mu\text{m}$  air gap, lens assembly shows mechanical stability with temperature. On increasing temperature, the air gap was found to decrease due to the expansion of the IG6 core and Ge shells. As the incident angles increase, the transmittance decreases but for temperatures above  $30^\circ\text{C}$  the transmittance followed an increasing trend due to increased effective optical length for wider incident angle. For normal incidence, the average transmittance was calculated to be 49.5 %. The average transmittance over all wavelengths and all angles peaked to 37% but it increased sharply to  $\sim 45\%$  at  $40^\circ\text{C}$ . The temperature variation also affects the focal spot sizes and focal lengths due to varying refractive indices of IR glasses. Importantly, with the variation in temperature,

incidence angle, and wavelength, the average transmittance, focal length, and spot size (*rms*) change. In addition, we have proposed a robust alternative to conventional ARCs as meta-structures which exhibited transmittance  $\sim 90\%$  through the Ge-IG6 with different airgaps interface. With the optimized shape and sizes of the metasurface, even higher transmittance can be achieved for IR radiation for a wide field-of-view.

**Acknowledgments:** This research is supported by CARS project provided by IRDE, Dehradun, India. Manish Kala wishes to acknowledge Council for Scientific and Industrial Research (CSIR), India for senior research fellowship. Pawan Singh thanks Indian Institute of Technology Roorkee, India for financial support.

**Conflict of Interest:** Authors declare no conflict of interest.

## References

- 1) J. Zhang, T. Qin, Z. Xie, L. Sun, Z. Lin, T. Cao, and C. Zhang, "Design of Airborne Large Aperture Infrared Optical System Based on Monocentric Lens," *Sensors*, 9907, 22(24), (2022).
- 2) A. Česnulevičius, A. Baurėnas, L. Bevainis, D. Ovodas, "A comparison of the influence of vegetation cover on the precision of an UAV 3D model and ground measurement data for archaeological investigations: A case study of the Lepelionys Mound, Middle Lithuania," *Sensors*, 5303, 19, (2019).
- 3) L. Huang, L. Liu, L. Jiang, T. Zhang, "Automatic mapping of thermokarst landforms from remote sensing images using deep learning: A case study in the northeastern Tibetan Plateau," *Remote Sens*, 2067, 10, (2018).
- 4) P. Velusamy, S. Rajendran, R. K. Mahendran, S. Naseer, M. Shafiq, J. G. Choi, "Unmanned aerial vehicles (UAV) in precision agriculture: Applications and challenges," *Energies*, 15, 217, (2021).
- 5) A. Fedele, R. Somma, C. Troise, K. Holmberg, G. De Natale, F. Matano, "Time-lapse landform monitoring in the Pisciarelli (Campi Flegrei-Italy) fumarole field using UAV photogrammetry," *Remote Sens*, 13, 118, (2020).
- 6) I. Stamenov, A. Arianpour, S. J. Olivas, I. P. Agurok, A. R. Johnson, R. A. Stack, R. L. Morrison, and J. E. Ford, "Panoramic monocentric imaging using fiber-coupled focal planes," *Optics Exp.* 31708, 22, (2014).
- 7) A. W. Lohmann, "Scaling laws for lens systems," *Appl. Opt.*, 28(23), 4996-4998, 1989.
- 8) O. Cossairt, D. Miao, S. K. Nayar, "Gigapixel Computational Imaging," *IEEE, International Conference on Computational Photography*, 2011.
- 9) D. L. Marks, E. J. Tremblay J. E. Ford, and D. J. Brady, "Microcamera aperture scale in monocentric gigapixel cameras," *Appl. Opt.*, 50(30), 5824, 2011.
- 10) D. J. Brady, *Optical Imaging and Spectroscopy*, Wiley, Optical Society of America, 2009.
- 11) D. J. Brady and N. Hagen, "Multiscale lens design," *Opt. Express* 17, 10659, 2009.
- 12) E. J. Tremblay, D. L. Marks, D. J. Brady, and J. E. Ford, "Design and Scaling of Monocentric Multiscale Imagers," *Appl. Opt.*, 51(20), 4691, 2012.
- 13) R. Kingslake, *A History of the Photographic Lens*, Academic, 49, 1989.
- 14) J. E. Ford and, E. Tremblay, "Extreme form factor imagers," *Imaging Systems*, OSA Technical Digest (CD) (2010), paper IMC2.

- 15) D. J. Brady, M. E. Gehm, R. A. Stack, D. L. Marks, D. S. Kittle, D. R. Golish, E. M. Vera, and S. D. Feller, "Multiscale gigapixel photography," *Nature* 486, 386–389 (2012).
- 16) Y. H. Huang, Y. G. Fu, G. Y. Zhang, and Z. Y. Liu, "Modeling and analysis of a monocentric multi-scale optical system," *Optics Express*, 32657, 28, (2020).
- 17) C. Gardner, *J. Research Nat. Bur. Stand.* 39, 213 (1947).
- 18) M. Reiss, "Notes on the Cos4 Law of Illumination," *J. Opt. Soc. Amer.*, 38(11), 1948.
- 19) I. Stamenov, I. P. Agurok, and J. E. Ford, "Optimization of two-glass monocentric lenses for compact panoramic imagers: general aberration analysis and specific designs," *Appl. Opt.*, 51, 7648, 2012.
- 20) T. S. Axelrod, N. J. Colella, and A. G. Ledebuhr, "The wide-field-of-view camera," *Energy and Technology Review*, (Lawrence Livermore National Laboratory, 1988).
- 21) I. Stamenov, I. P. Agurok, and J. E. Ford, "Optimization of high-performance monocentric lenses," *Appl. Opt.*, 52, 8287, 2013.
- 22) Y. Shen Sr., H. Wang, Y. Xue, M. Liu, Y. Jie, S. Lin, and J. Liu, "Design of concentric multiscale optical system for long-wave infrared band", *Proc. SPIE 11567, AOPC 2020, Optical Sensing and Imaging Technology*, 115673Z 2020.  
<https://doi.org/10.1117/12.2580270>
- 23) M. Uniyal, R. Mandal, and P.K. Sharma, "Optical design of a multiscale imager in 8 to 12  $\mu$  m spectral band using monocentric lens," *Optical Engineering*, 62, 105104-105104, 2023.
- 24) [https://www.vitron.de/files/VITRON\\_IG-6\\_Datenblatt\\_Okt\\_2020\\_1\\_.pdf](https://www.vitron.de/files/VITRON_IG-6_Datenblatt_Okt_2020_1_.pdf)
- 25) N. P. Barnes and M. S. Piltch, "Temperature-dependent Sellmeier coefficients and nonlinear optics average power limit for germanium", *Opt. Soc. Am.*, 69, 1979.
- 26) COMSOL Multiphysics Reference Manual, version 5.3", COMSOL, Inc, [www.comsol.com](http://www.comsol.com)
- 27) See Supplemental Material, "SupplementaryFile"
- 28) H. H. Li, "Refractive index of ZnS and its wavelength and temperature derivatives," *Journal of Physical and Chemical, Reference Data*, 13, 103, 1984.
- 29) X. Zhang and A. L. Bradley, "Wide-angle invisible dielectric metasurface driven by transverse Kerker scattering," *Phys. Rev. B*, 103, 195419, 2021

## Supplementary

### Optimization of airgap in a monocentric lens assembly and metasurface based anti-reflecting coating in the long-wave IR regime

Manish Kala<sup>1</sup>, Pawan Singh<sup>1</sup>, Sanjay Kumar Mishra<sup>2</sup>, Unnikrishnan Gopinathan<sup>2</sup>, Ajay Kumar<sup>2</sup>, Akhilesh Kumar Mishra<sup>1,3\*</sup>

<sup>1</sup>Department of Physics, Indian Institute of Technology Roorkee, Roorkee-247667, Uttarakhand, India

<sup>2</sup>Photonics Research Lab, Instruments Research and Development Establishment, Dehradun 248008, India

<sup>3</sup>Centre for Photonics and Quantum Communication Technology, Indian Institute of Technology Roorkee, Roorkee-247667, Uttarakhand, India

\*Corresponding author: [akhilesh.mishra@ph.iitr.ac.in](mailto:akhilesh.mishra@ph.iitr.ac.in)

#### S1. Variation of Spots with incident angle for different wavelengths

Here, we discuss the spatial shifts of spot diagram on image surface at  $10\mu\text{m}$  wavelength for different incident angles. Figures S1-S8 show spatial shifts & rms value of the size of spot diagram on the image plane at  $0^\circ$ ,  $2^\circ$ ,  $4^\circ$ ,  $6^\circ$ , and  $8^\circ$  incident angles. Colorbars show intensity variation at these spots for different rays.

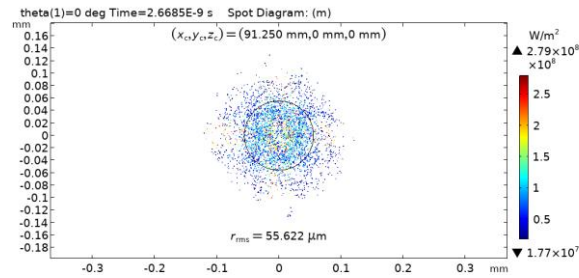


Fig. S1: Spot diagram at image surface at  $\theta = 0^\circ$ .

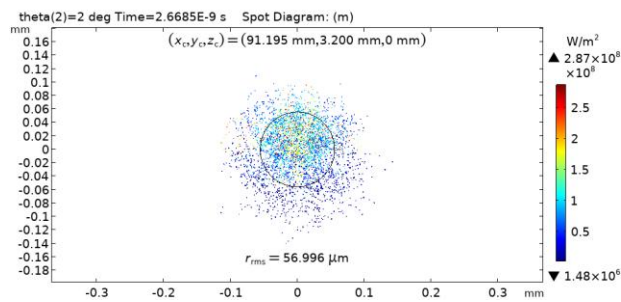


Fig. S2: Spot diagram at image surface at  $\theta = 2^\circ$ .

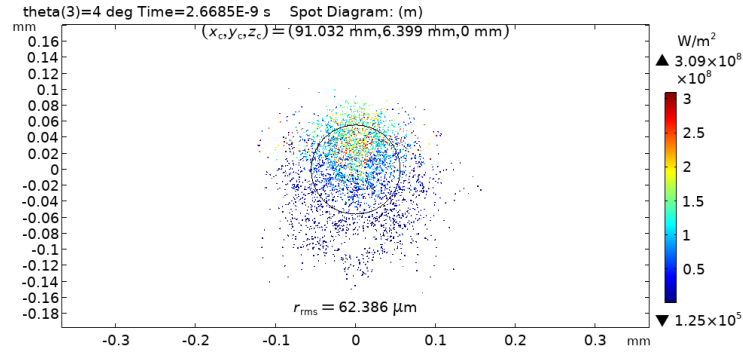


Fig. S3: Spot diagram at image surface at  $\theta = 4^\circ$ .

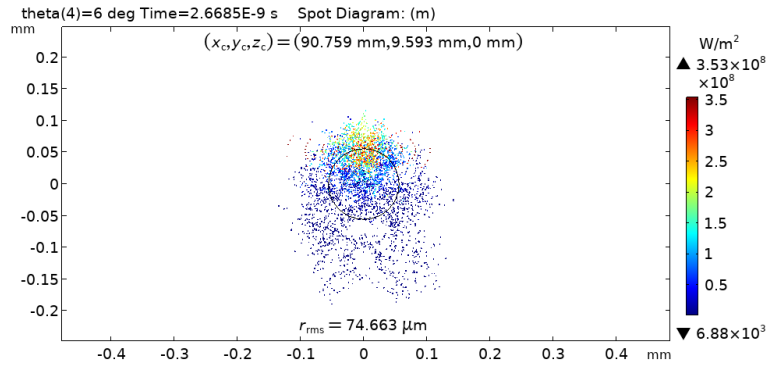


Fig. S4: Spot diagram at image surface at  $\theta = 6^\circ$ .

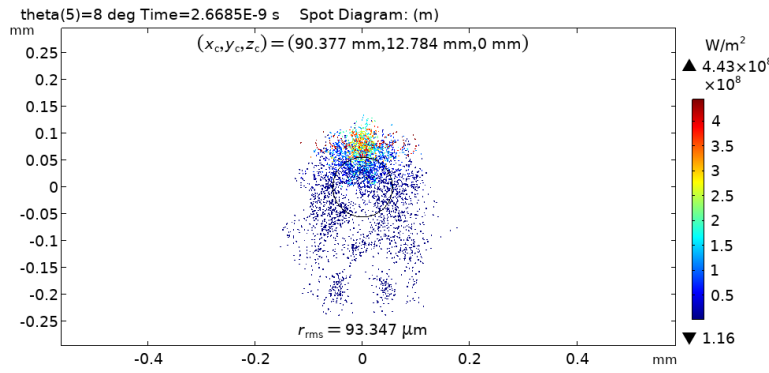


Fig. S5: Spot diagram at image surface at  $\theta = 8^\circ$ .

## S2. Transmittance of the lens assembly for different incidence angles at different wavelengths

In this section, we study the transmittance through the lens assembly at different wavelengths for different incident angles. Figures S6-S10 depict the transmittance variation with rising temperature at different wavelengths for  $0^\circ$ ,  $2^\circ$ ,  $4^\circ$ ,  $6^\circ$  and  $8^\circ$  incident angles. From the figures, we notice that the transmittance decreases with increase in the incident angles.

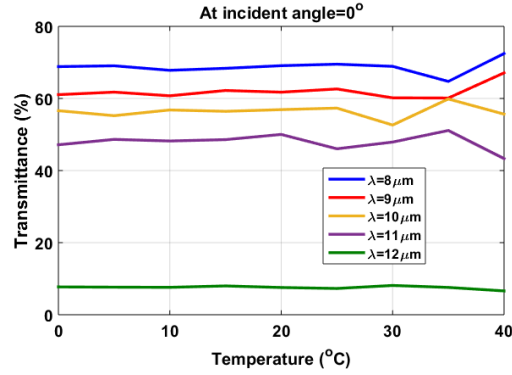


Fig. S6: Transmittance variation with temperature at  $\theta = 0^\circ$ .

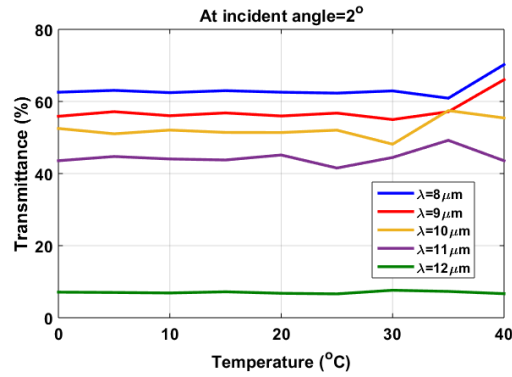


Fig. S7: Transmittance variation with temperature at  $\theta = 2^\circ$ .

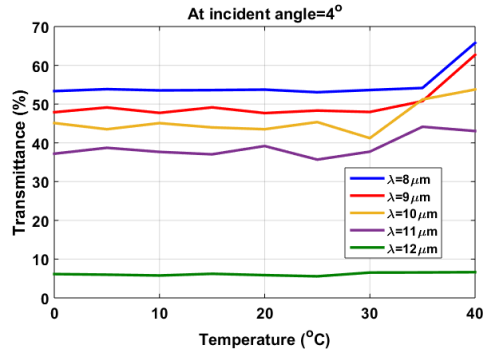


Fig. S8: Transmittance variation with temperature at  $\theta = 4^\circ$ .

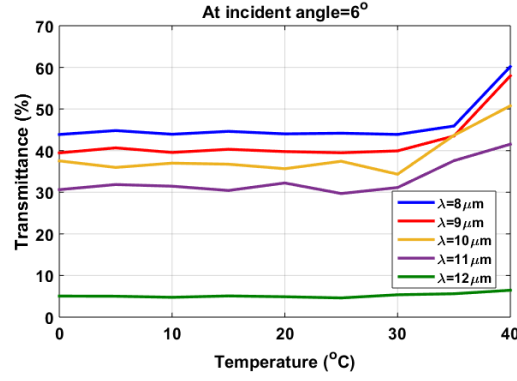


Fig. S9: Transmittance variation with temperature at  $\theta = 6^\circ$ .

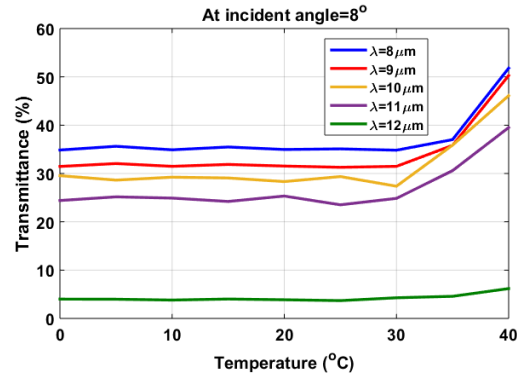


Fig. S10: Transmittance variation with temperature at  $\theta = 8^\circ$ .

### S3. Variation of the spot diagrams with temperature and incident angles

In this section, we show the variation in the spot size and its spatial shift with increasing temperature from 273K-313K (0 to 40°C). Figures S11-S19 reveals that spot diagram for 10 $\mu\text{m}$  wavelength shift on image surface and  $r_{\text{rms}}$  values of radius also changes accordingly as mentioned in the figures.

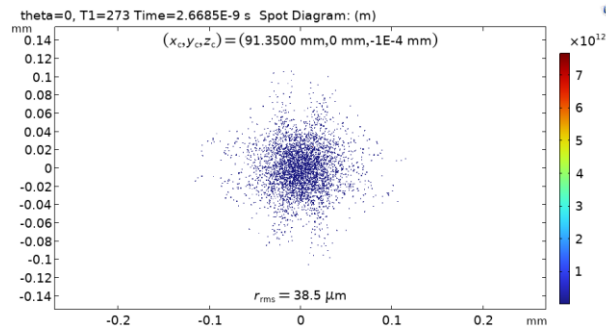


Fig. S11: Spot diagram at image surface at temperature 0°C (273 K).

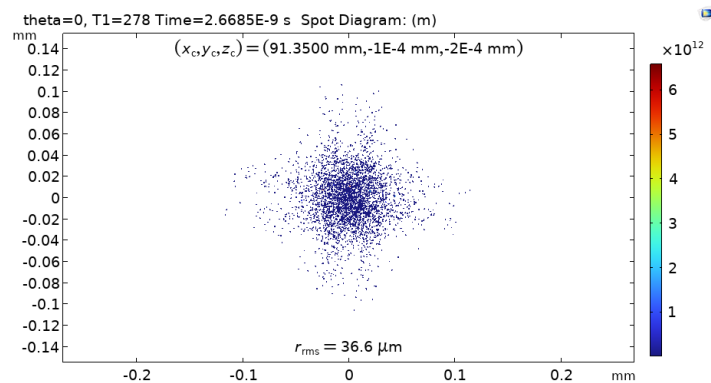


Fig. S12: Spot diagram at image surface at temperature  $5^{\circ}\text{C}$  (278 K).

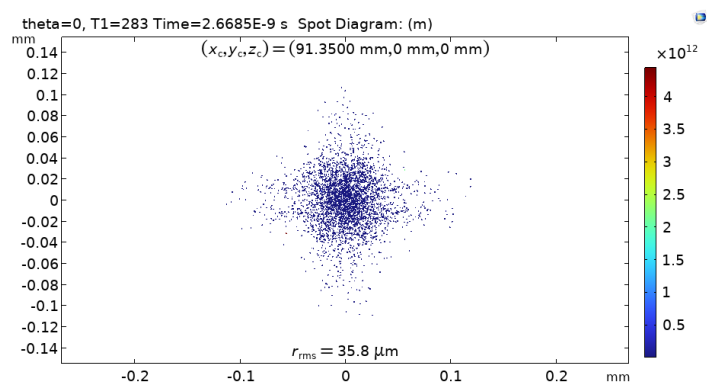


Fig. S13: Spot diagram at image surface at temperature  $10^{\circ}\text{C}$  (283 K).

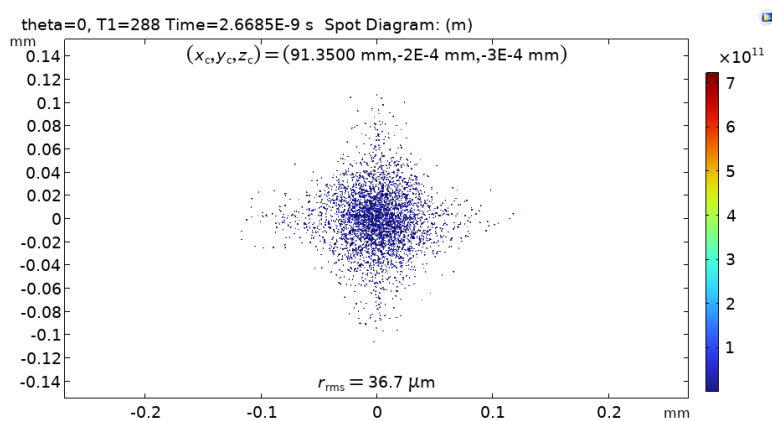


Fig. S14: Spot diagram at image surface at temperature  $15^{\circ}\text{C}$  (288 K).

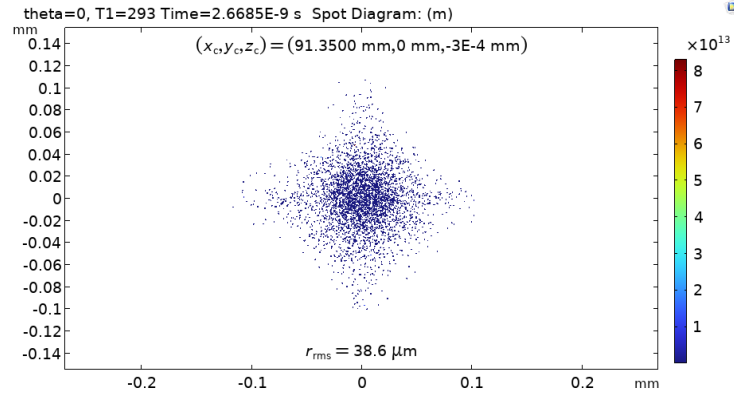


Fig. S15: Spot diagram at image surface at temperature  $20^{\circ}\text{C}$  (293K).

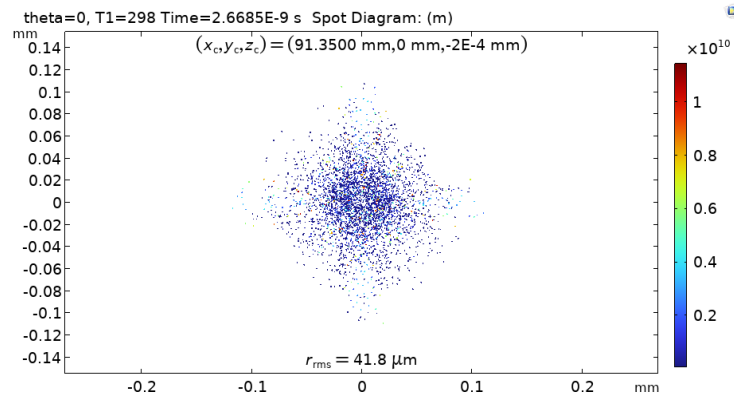


Fig. S16: Spot diagram at image surface at temperature  $25^{\circ}\text{C}$  (293 K).

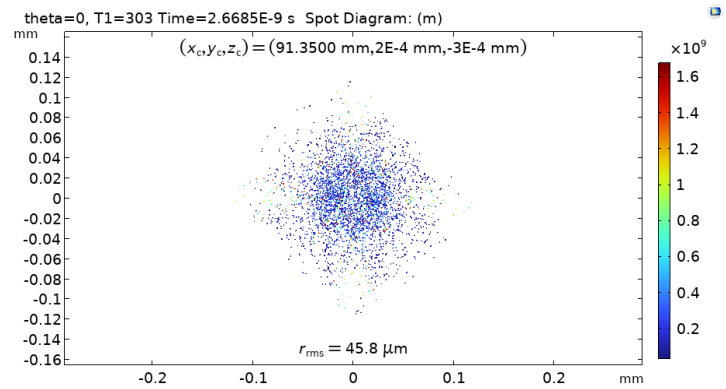


Fig. S17: Spot diagram at image surface at temperature  $30^{\circ}$  (303 K).

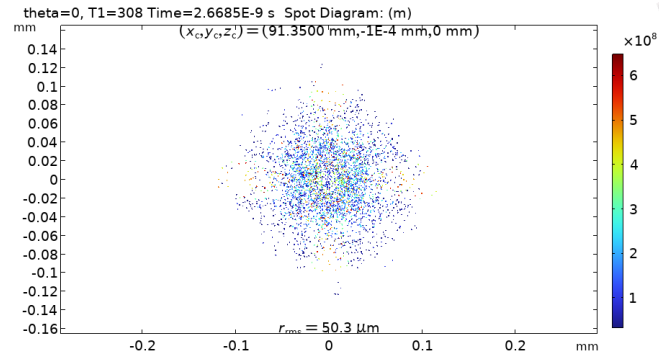


Fig. S18: Spot diagram at image surface at temperature  $35^\circ$  (308 K).

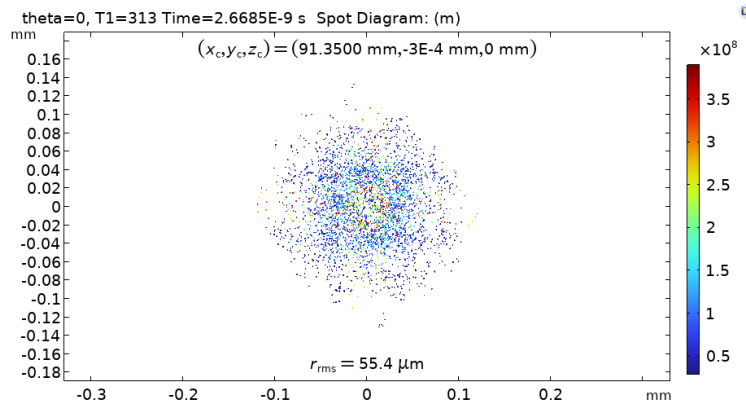


Fig. S19: Spot diagram at image surface at temperature  $40^\circ$  (313 K).

#### S4. Variation of the focal length of the monocentric lens assembly with temperature and incident angles

In this section, we discuss the variation in focal length of the lens assembly with temperature and incidence angle. With increase in temperature, focal length increases, while it decreases with incident angles as reported in Table S1.

Table S1: Variation in focal length with temperature and incident angles.

S. No .	$T$ ( $^{\circ}C$ )	Calculated focal length (mm) at 10 $\mu m$ wavelength for different incident angles ( $\theta$ )								
		$0^{\circ}$	$1^{\circ}$	$2^{\circ}$	$3^{\circ}$	$4^{\circ}$	$5^{\circ}$	$6^{\circ}$	$7^{\circ}$	$8^{\circ}$
1	0	91.287	91.266	91.241	91.187	91.089	91.001	90.884	90.739	90.571
2	5	91.316	91.302	91.276	91.219	91.154	91.032	90.918	90.772	90.604
3	10	91.344	91.335	91.303	91.256	91.178	91.065	90.952	90.802	90.636
4	15	91.373	91.365	91.335	91.286	91.215	91.098	90.992	90.833	90.667
5	20	91.407	91.399	91.376	91.323	91.246	91.131	91.016	90.866	90.699
6	25	91.440	91.427	91.403	91.356	91.280	91.167	91.048	90.901	90.731
7	30	91.497	91.465	91.403	91.385	91.312	91.201	91.078	90.931	90.764
8	35	91.512	91.502	91.470	91.418	91.338	91.233	91.110	90.965	90.795
9	40	91.556	91.535	91.503	91.454	91.369	91.265	91.142	90.998	90.827